The Effect of Friction Stir Processing on the Microstructure and Mechanical Properties of an Aluminum Lithium Alloy

TANYA L. GILES, KEIICHIRO OH-ISHI, ALEXANDER P. ZHILYAEV, SRINIVASAN SWAMINATHAN, MURRAY W. MAHONEY, and TERRY R. McNELLEY

Friction stir processing (FSP) was conducted on a wrought plate of AA2099 to refine and homogenize the microstructure and enhance the through-thickness ductility and fracture resistance. Optical microscopy (OM), orientation imaging microscopy (OIM), and transmission electron microscopy (TEM) methods were employed to evaluate microstructure and microtexture in as-received material and in material subjected to FSP as well as postprocessing heat treatments. Hardness and orientation-dependent tensile test data were combined with anticlastic bending fatigue data to characterize the as-received, processed, and processed and heat-treated conditions of the material.

DOI: 10.1007/s11661-008-9698-8

I. INTRODUCTION

THE addition of lithium increases the elastic modulus and decreases the density of aluminum. Binary Al-Li alloys may be strengthened by intragranular precipitation of coherent spheroidal $\delta'(Al_3Li)$ particles during aging after solution heat treatment. The δ' is an $L1_2$ phase and the close correspondence of its lattice with that of the fcc α phase results in small misfit strains and, in turn, a homogeneous distribution of the δ' when the alloy is solution treated and briefly aged below the δ' solvus.[1,2] The δ' precipitate particles harden the alloy but they may also be sheared by moving dislocations and the resulting slip planarity may result in poor ductility. The equilibrium $\delta(AlLi)$ phase is believed to nucleate heterogeneously and independently of δ', and apparently grows by dissolution of the surrounding metastable δ' after relatively long aging times.[3]

Because the binary alloys exhibit poor ductility and fracture toughness, structural Li-containing Al materials are based on the ternary Al-Cu-Li system and also contain Mg, Zr, and Mn additions. The Cu and Mg have been shown to reduce the solubility of Li and enhance the precipitation of various phases more resistant to shearing, thus producing an effective strengthening increment.[2,4,5] Coprecipitation of the metastable strengthening phases $T_1(Al_2CuLi)$, $T_2(Al_6Cu(LiMg)_3)$, and $\theta'(Al_2Cu)$ takes place along with the precipitation of $\delta'(Al_3Li)$ during peak aging of such alloys.[6,7] Each of these strengthening phases competes for nucleation sites and the Cu and Li solutes.[8] The Zr affects precipitation kinetics and is added in combination with Mg to enhance the age-hardening response as well as toughness and corrosion resistance.[4] Also, the Zr additions lead to the formation of coherent $\beta'(Al_3Zr)$ dispersoids that inhibit recrystallization during hot rolling and lead to formation of pancake-shaped grains. The Mn results in formation of large incoherent particles that may act as nucleation sites for recrystallization.[2,5] Thus, microstructures in engineering Al-Li alloys may typically include a variety of metastable intragranular phases, such as $T_1(Al_2CuLi)$, and $\beta'(Al_3Zr)$, as well as the intergranular equilibrium phases such as $T_2(Al_6CuLi_3)$ and $\delta(AlLi)$.

Barriers to replacement of high-strength AA7XXX materials with Li-containing aluminum alloys have included lower thermal stability at high lithium content, greater anisotropy, and higher cost. Furthermore, the Al-Li alloys often exhibit poor short-transverse (ST, *i.e.*, through-thickness) properties and unpredictable fatigue crack growth behavior. Specifically, low ST fracture toughness reflects brittle intergranular fracture (BIF) leading to delamination at stress concentrators such as holes and rivets, making failure assessments difficult. Possible causes of BIF have been proposed,[5,9,10] although the details of the mechanisms have not been determined.

Significant advances have been made in reducing mechanical anisotropy while maintaining ductility and strength by adjusting alloy chemistries and thermomechanical treatments. Alloy development has also focused on controlling microstructural evolution to reduce grain

TANYA L. GILES, formerly Graduate Student, Naval Postgraduate School, is Chief with the Machinery Branch, Marine Safety Center, United States Coast Guard, Washington, DC 20593. KEIICHIRO OH-ISHI, Postdoctoral Fellow, is with the National Institute for Materials Science, Tsukuba, Ibaraki 305-0047, Japan. ALEXANDER P. ZHILYAEV, Research Scientist, is with the Institute for Metals Superplasticity Problems, RAS, Ufa 450001 Russia. SRINIVASAN SWAMINATHAN, formerly NRC Postdoctoral Fellow, Center for Materials Science and Engineering, Department of Mechanical and Astronautical Engineering, Naval Postgraduate School, is Research Scientist, GE Global Research, Bangalore 560066, India. Contact email: tmcnelley@nps.edu MURRAY W. MAHONEY, formerly with Rockwell (now Teledyne) Scientific Company, Thousand Oaks, CA 91360, is a Consultant. TERRY R. McNELLEY, Distinguished Professor, is with the Center for Materials Science and Engineering, Department of Mechanical and Astronautical Engineering, Naval Postgraduate School, Monterey, CA 93943-5146.

Manuscript submitted April 7, 2008.
Article published online November 18, 2008

boundary precipitation and limit inhomogeneities such as coarse constituents or precipitate-free zones (PFZs).[8] AA2099 is one such alloy; it is precipitation hardened by θ', $T1$, β', and δ' phases. The θ' phase is a semicoherent precipitate with a tetragonal structure that grows as thin plates on the $\{001\}\alpha$ planes, whereas the hexagonal $T1$ platelets appear on the $\{111\}\alpha$. The spherical β' phase is typically 10 to 50 nm in diameter and is homogenously dispersed in the matrix. However, β' can occasionally be seen at high-angle grain boundaries.[4] The δ' phase nucleates and grows on Guinier-Preston (GP-I) zones.[8,11,12]

In the present study, the potential for further property improvements through friction stir processing (FSP) of wrought AA2099 has been examined. This method is an adaptation of friction stir welding and involves use of a cylindrical wear-resistant tool that has a larger diameter shoulder and a concentric smaller-diameter pin. The tool is rotated while the pin is pressed into the surface of a metallic material. A combination of frictional and adiabatic heating due to contact conditions at the tool-workpiece interface leads to localized heating and softening of the material, and to steep gradients in strain, strain rate, and temperature within a processed (stir) zone that develops around the pin as it penetrates the surface. When the tool shoulder comes in contact with the surface, the tool is then traversed along a path to process a region of interest. The tool shoulder acts to constrain upward flow of material while severe plastic deformation in the stir zone results in movement of material about the pin.[13] The thermomechanical cycle induced by FSP may result in localized homogenization and refinement of the microstructure that leads to improved mechanical properties in the volume of material that has experienced processing.[13,14] In the present study, an as-received AA2099-T8 plate was subjected to FSP using a rectangular raster pattern. The resulting microstructures were analyzed by various techniques and compared to that of the as-received plate. Orientation-dependent tensile properties were determined using miniature tensile samples and anti-clastic bending fatigue tests were employed to assess fatigue and failure due to delamination cracking.

II. EXPERIMENTAL PROCEDURES

For this study, two plates, each approximately 580 × 380 × 13 mm in size, were sectioned from rolled AA2099 plate that had been processed to a –T8 temper (provided by Rockwell (now Teledyne) Scientific Corporation). The largest dimension was along the prior rolling direction (RD) and the reference axes, *i.e.*, RD, TD (direction transverse to the rolling direction in the plane of the plate), and ND (the plate normal direction), have been retained throughout the current work. Chemical analysis on the material was conducted by Anamet Inc. (Hayward, CA) and the results are provided in Table I. Friction stir processing was conducted at Rockwell using a tool fabricated with MP159 (composition: 25Ni-36Co-19Cr-9Fe-7Mo-3Ti wt pct). The tool had a shoulder 25 mm in diameter and a threaded pin 12.7 mm in diameter and 12.5 mm in depth. Processing was conducted at 400 revolutions per minute (rpm) and a traversing speed of 127 mm m^{-1}, *i.e.*, 5 inches per minute (ipm), and with the tool tilted ~3 deg away from the direction of tool advance. An area of the plate about 520 × 320 mm^2 in size was processed in a rectangular spiral pattern. The initial pass was along the centerline in the plate RD and successive traverses were offset by 4.5 mm. The advancing side of the tool (tangential velocity at the tool surface is parallel to the direction of tool advance) was always to the outside of the spiral pattern. Approximately 100 days elapsed between processing and the commencement of subsequent analysis, and this precluded assessment of natural aging in the stir zone and adjacent thermomechanically-affected zone during this interval.

Table I. Chemical Composition Analysis of the As-Received Plate

Element	Al	Cu	Li	Zn	Mg	Mn	Zr
Concentration in wt pct	bal	2.30	1.66	0.56	0.20	0.30	0.08

Samples for optical microscopy (OM) were prepared by metallographic polishing followed by etching with Keller's reagent. For orientation imaging microscopy (OIM) analysis, samples were sectioned to reveal the RD-ND plane for both the as-received and FSP material, polished using diamond abrasives and then finished by electropolishing with a 33 pct nitric acid-67 pct methanol solution initially cooled to –25 °C. A Topcon SM-510 (Topcon Technologies, Inc., Paramus, NJ) scanning electron microscope (SEM) operating with a tungsten filament at an accelerating voltage of 20 kV and utilizing EDAX-TSL software (AMETEK, Paoli, PA) was used for OIM data collection and analysis. A standard clean-up procedure[15] was employed. Transmission electron microscopy (TEM) was accomplished with a Topcon 002B instrument operating at 200 kV. Samples for TEM examination were obtained by first sectioning with a low-speed diamond saw to obtain a slice aligned with the RD-ND plane for both the FSP and as-received material. Disks 3 mm in diameter were then punched from this slice at a location 3 to 6 mm below the surface; for the plate subjected to FSP, this was the surface in contact with the tool. These disks were subsequently thinned to perforation by electropolishing using a 33 pct nitric acid, 67 pct methanol solution initially cooled to −25 °C.

Hardness, tensile, and anticlastic bending tests were also conducted. For hardness measurements, the RD-ND planes of all the samples were metallographically polished to mirrorlike finish, three Rockwell 'B' scale measurements were performed and averaged at each location. Tensile samples conforming to ASTM E-8 were sectioned using a Charmilles–Andrew EF630 (Charmilles-Andrew, Minnetonka, MN) electrodischarge machine (EDM) employing a 0.3-mm diameter brass wire and then ground with 1000 grit SiC paper on all surfaces to remove machining damage. Samples having tensile axes aligned with either the RD or the TD

were prepared at a depth of ~6.5 mm from the surface of the plate. This depth corresponds to the middle of the processed (stir) zone after FSP. The gage dimensions of these samples were 15.7-mm length × 1.7-mm width × 1.0-mm thickness. Miniature tensile samples having gage sections 2.5-mm length × 1.0-mm width × 1.0-mm thickness were employed for testing along the ND of the plate. Tensile tests for the RD and TD orientations were conducted to failure at a constant crosshead speed of 1.0 mm m^{-1} using a computer-controlled Instron model 4507 machine (Instron, Norwood, MA), while the miniature specimens were tested in tension at the same crosshead speed using a laboratory benchtop machine. The EDM was also used to prepare anticlastic bending specimen coupons from the as-received and FSP plates. The specimen design is shown in the Appendix in Figure A1(a). Anticlastic bending involves the application of equal but opposite bending moments at the diagonal corners of a square plate (Figure A1(b)). The distributions of normal and shear stresses through the plate thickness as a consequence of anticlastic bending are illustrated in Figure A1(c). With appropriate fixtures and fully-reversed cyclic loading the normal stresses alternate in sign and direction through the thickness of the plate, while the maximum shear stress alternates in direction on the coupon midplane. Accordingly, the anticlastic specimens were prepared so that the specimen neutral plane corresponded to the midplane of the as-received and FSP plates. Furthermore, the coupons were sectioned such that the bending moments would be perpendicular and parallel to the prior RD of the plate. Holes were drilled and samples ground with 1000 grit SiC paper to remove damage due to EDM. All samples were checked for macroscopic defects prior to testing. Anticlastic testing in a cyclic mode was performed using the Instron model 4507 machine at a constant traversing rate of 63.5 mm min^{-1} (2.5 in. min^{-1}). Loading was fully reversed and load ranges were ± 3338 N (750 lbs), ± 4451 N (1000 lbs), and ± 6676 N (1500 lbs). Cycles-to-failure and fracture modes were recorded for each specimen. Microstructure, microtexture, hardness and tensile properties were also determined for samples of the FSP material reaged at 148 °C for different times and air cooled to room temperature.

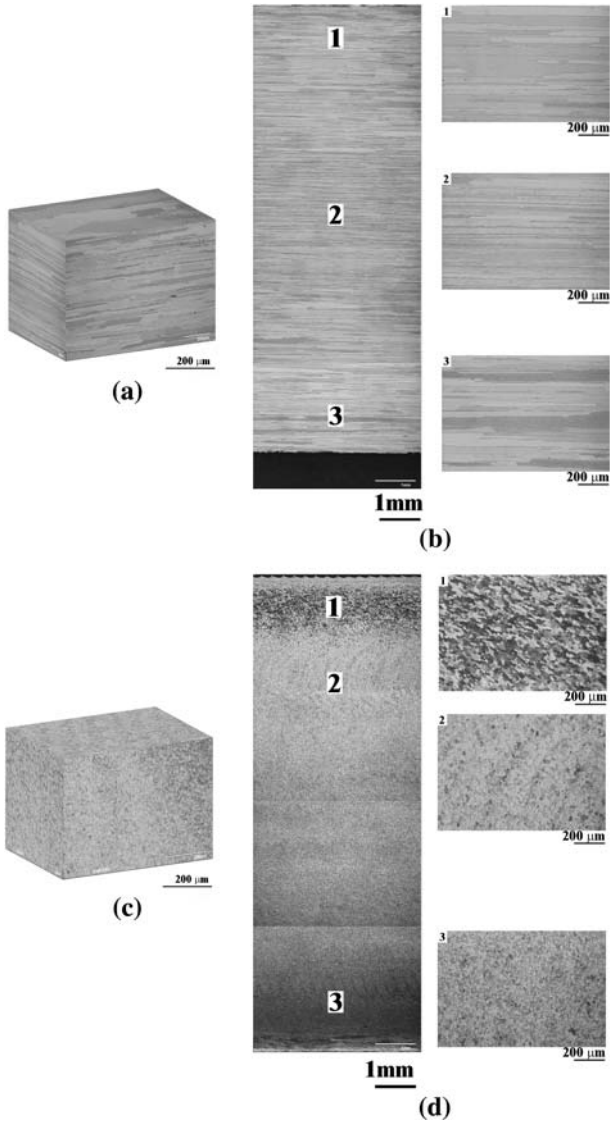

Fig. 1—(*a*) Triplanar OM view of as-received plate, (*b*) higher resolution optical images from RD-ND plane, (*c*) triplanar OM view of FSP plate, and (*d*) higher magnification optical images from the prior RD-ND plane.

III. RESULTS

A. *Microstructure*

1. *Optical microscopy*

The isometric representation in Figure 1(a) for the as-received plate shows highly elongated pancake-shaped grains and wide variations in grain thickness and aspect ratio typical of wrought aluminum alloys produced by rolling. A decrease in average grain thickness from the surface to the midplane along the ND is apparent in Figure 1(b). In contrast, the intense plastic deformation and adiabatic heating in the volume of material subjected to the thermomechanical cycle of the FSP have resulted in the formation of a fine-grained recrystallized microstructure in processed material. This is clear in the isometric illustration in Figure 1(c) where the flattened pancake-shaped grains of the as-received plate (Figure 1(a)) have been replaced with equiaxed grains in all three orthogonal planes of view. However, bandlike features typical of FSP are also evident and the grain size is coarsest near the surface in contact with the tool shoulder and finest away from the shoulder. This may be seen in the micrographs in Figure 1(d). Where visible in Figure 1(d), the spacing between the bandlike features is 0.2 to 0.5 mm, while the tool advance per revolution is ~0.31 mm. These bandlike features remained apparent after post-FSP aging treatments.

2. *Orientation Imaging Microscopy*

Orientation imaging microscopy data for the as-received plate are presented in Figure 2(a) in the form of an orientation image obtained from the RD-ND

plane. The inset orientation color key corresponds to the specimen normal in Figure 2. The high-angle boundaries (misorientation ≥15 deg) are delineated by the heavy black lines in this image. The individual orientations are also plotted in pole figures wherein the data are also presented in the RD-ND plane of the as-received plate. These pole figures show a characteristic texture of a rolled fcc polycrystalline material comprising mainly β-fiber orientations. The misorientation distribution is consistent with distributions reported for rolled Al-Cu-Zr alloys where the high-angle boundaries correspond to interfaces between texture variants.[16] Orientation images, pole figures, and misorientation distributions from the plate that had been subjected to FSP are shown in Figures 2(b), (c), and (d) for the top (in contact with the tool shoulder), middle, and bottom regions of the stir zone, respectively. These data were acquired from a plane in the stir zone corresponding to the RD-ND plane of the prior as-received plate. Examination of the orientation images reveals that the grain size decreases along the ND upon traversing downward from the surface in contact with the tool shoulder. The area-weighted grain sizes for the images shown in Figures 2(b), (c), and (d) are 20.2, 16.2, and 13.7 μm, respectively. The orientation data have also been plotted as pole figures in the same plane as that of the orientation images. The texture is a characteristic *B*-fiber shear texture, similar to that reported after FSW of similar alloys.[17–19] This alignment is most apparent at the middle of the stir zone (Figure 2(c)) and is consistent with the shear deformation induced by rotation of the pin. The apparent rotational symmetry about an axis nearly aligned with the ND suggests that the shear plane is a cylindrical plane that is coaxial with the tool with the shear direction being tangential to the cylinder surface and perpendicular to the tool axis. The misorientation distributions from the top and middle of the stir zone are consistent with the presence of strong orientation fibers, although the fraction of low-angle boundaries exceeds that expected for a fiber texture. A random component in the texture is most apparent in the pole figures as well as the misorientation distribution from the bottom of the stir zone. Altogether, the microstructure and microtexture data for the FSP plate reflect evolution of microstructure predominantly by a continuous recrystallization reaction during FSP, although random orientations near the bottom of the stir zone may reflect a contribution from other recrystallization processes. Little effect of heat treatment at 148 °C after FSP was apparent in OIM analysis.

3. *Transmission Electron Microscopy*

Figure 3 shows bright-field (BF)/dark-field (DF) pairs from TEM analysis of the as-received plate, the material subjected to FSP, and the material following reaging after FSP. The BF image in Figure 3(a) is consistent with OM and OIM observations in as-received material of elongated grains 2 to 10 μm in thickness and containing subgrains. The diffraction spot for DF imaging of the δ' precipitate is indicated in the inset selected area diffraction (SAD) pattern in the BF image, and the corresponding fine homogeneously-distributed δ' particles are apparent in the DF image (Figure 3(a)). After FSP, the microstructure exhibits coarse precipitate particles located on the grain boundaries, as seen in the BF image in Figure 3(b). These particles are present in greater amount and are larger in size in comparison to the as-received material. The SAD pattern and corresponding DF image indicate that the intergranular precipitates are the T_1 phase formed due to the overaging effect of the FSP thermomechanical cycle. The SAD analysis also revealed that elongated platelets apparent in the BF image had formed on the {111} planes of the matrix lattice while the fine δ' had reverted to solution. Figure 3(c) shows that the main effect of post-FSP aging at 148 °C for 24 hours is the reprecipitation of the fine δ' that was absent following FSP.

B. *Mechanical Properties*

1. *Hardness*

The hardness distribution as a function of depth along the thickness of the plate is shown in Figure 4 for the as-received plate, material subjected to FSP, and material subjected to FSP followed by aging at 148 °C for different times. The hardness of the as-received plate remains nearly constant at a value of ~80 HRB through the thickness of the plate. After FSP, the hardness decreases steeply from a value of 57 HRB in the stir zone near the surface in contact with the tool shoulder to a value of 23 HRB close to the bottom of the stir zone. Upon annealing for 0.24 hours to reage the material after FSP, the hardness of the stir zone decreases further to a value of ~30 HRB at the top surface while maintaining a hardness value of ~23 HRB at the bottom. On further increasing the annealing time, the hardness increases uniformly throughout the plate. Thus, after 72 hours annealing following FSP, the hardness value close to the surface is ~73 HRB while the hardness close to the bottom of the stir zone is ~59 HRB.

2. *Tensile tests*

Figure 5 summarizes results obtained from tensile testing for different orientations of samples prepared from as-received plate, after FSP, and FSP followed by the reaging treatment. The longitudinal (L) and transverse (T) samples were obtained at a depth of 6.5 mm from the surface in the as-received plate. The L and T samples after FSP were obtained from the same location relative to the surface of the processed plate, and so are at a location corresponding to the middle of the stir zone. Only the L orientation was used to determine tensile properties after reaging following FSP. The as-received plate properties are approximately isotropic in the plane of the plate but are distinctly poorer in the ST orientation. Thus, the yield strengths in the L and T orientations are 500 and 520 MPa, respectively, while the ST yield strength was 320 MPa. The ultimate tensile strength values of the as-received plates exhibited the same orientation dependence as the yield strength data while the ductility of the samples along L, T, and ST orientations were 6.2, 5.9, and 2.5 pct, respectively.

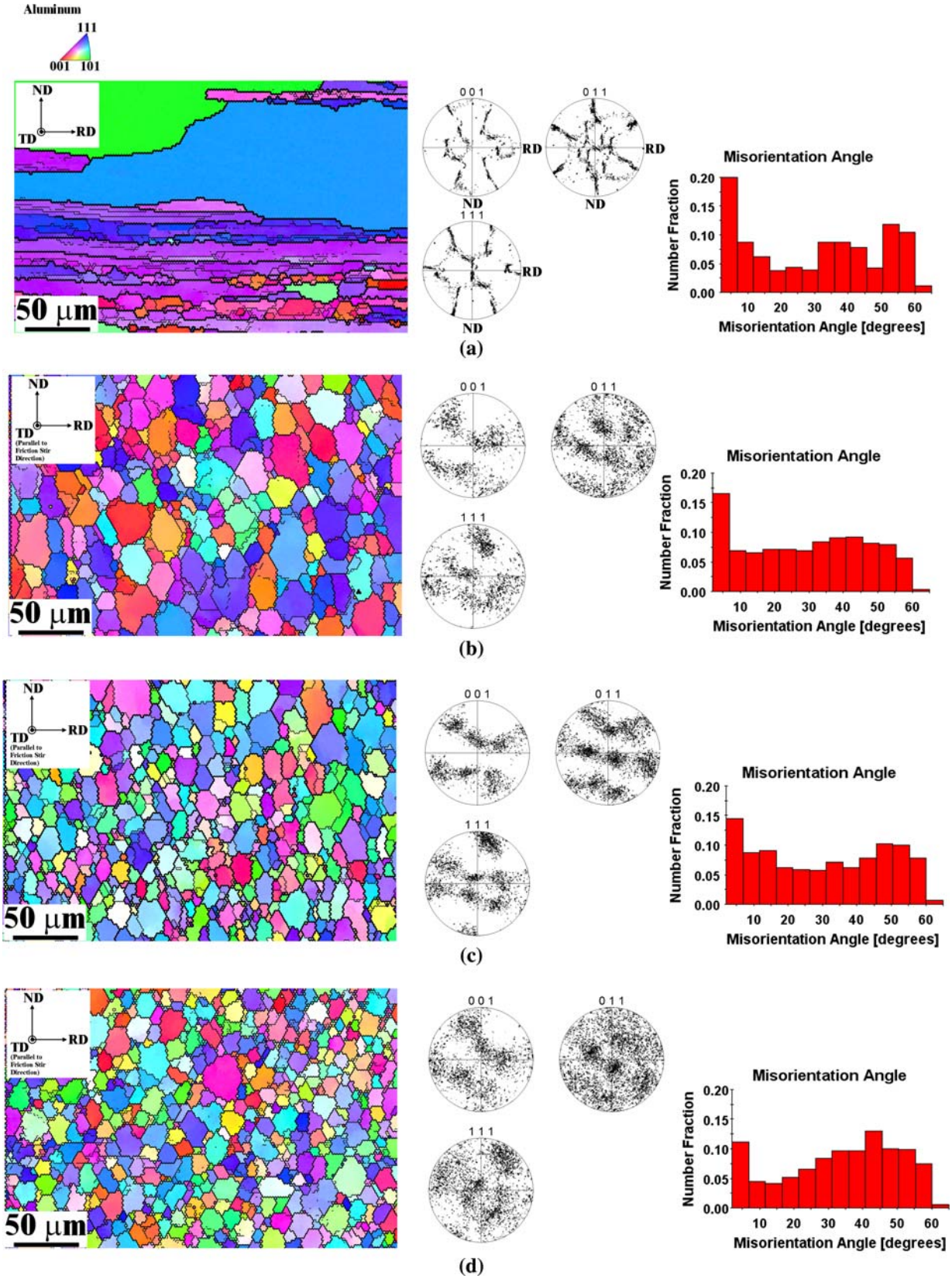

Fig. 2—IPF maps of RD-ND plane, pole figures, and misorientation angle distribution from RD-ND planes of (*a*) as-received condition and (*b*) top, (*c*) middle, and (*d*) bottom of stir zone after FSP.

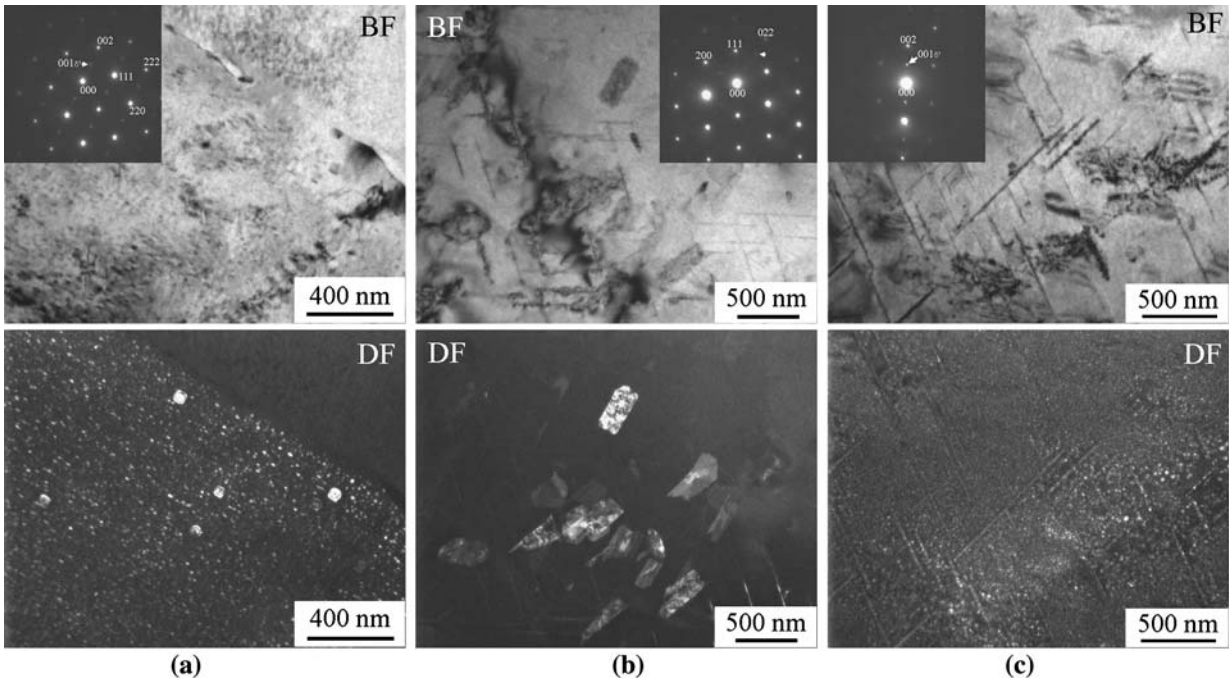

Fig. 3—BF and DF TEM images of AA2099: (*a*) as-received plate, (*b*) after FSP, and (*c*) FSP followed by heat treatment at 148 °C for 24 h.

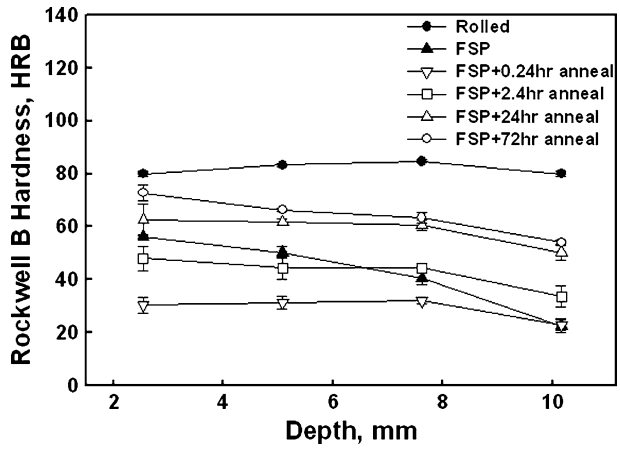

Fig. 4—Rockwell hardness as a function of depth for as-received AA2099-T8 plate, after FSP, and FSP followed by annealing at 148 °C for various times.

The FSP resulted in reduced yield and tensile strengths but improved ductility, especially in the ST orientation. The tensile testing revealed yield strengths of 270, 215, and 190 MPa in the L, T, and ST orientations, respectively, while the corresponding ultimate tensile strengths were 330, 310, and 250 MPa. However, in contrast to as-received materials, ductility was nearly isotropic after FSP: 8.6 pct (L), 7.1 pct (T), and 7 pct (ST). Reaging after FSP aging resulted in a yield strength of 295 MPa, tensile strength of 351 MPa, and ductility of 10 pct along the L orientation. A second tensile sample using the same heat treatment was allowed to naturally age at room temperature for 30 days prior to testing. No appreciable difference in yield or tensile strength was seen but a further increase in ductility by 2 pct was observed.

Tensile samples in L and T orientations from the as-received plate exhibited slant-type fracture surfaces nominally oriented at 45 deg to the loading axis and inclined through the thickness of the gage. In contrast, the ST specimens exhibited predominantly flat fracture surfaces perpendicular to the loading axis but with some necking apparent. In Figure 6(a), representative SEM fractography from the L orientation reveals separation along the boundaries of the elongated pancake grains. The resulting layered grains then exhibit necking with microvoid formation and coalescence on final rupture and so both intergranular and transgranular cracking is apparent in these samples. The fracture surfaces for FSP samples in all orientations were nominally oriented at 25 to 35 deg to the load axis. Some necking was also observed. Fractography revealed mostly intergranular fracture with some microvoid formation on the grain facets (Figure 6(b)). The extent of intergranular fracture is reduced in the L orientation samples after heat treatment at 148 °C for 24 hours following FSP (Figure 6(c)).

3. *Anticlastic bend testing*

Anticlastic bending test results for all samples tested are summarized in Table II. The maximum normal stresses were divided by the respective yield stress in the L orientation for each condition and the resulting normalized data are plotted in Figure 7. In this representation, FSP as well as post-FSP heat treatment increases the fatigue strength of this alloy. Thus, the as-received material failed at ~10^3 cycles at the highest

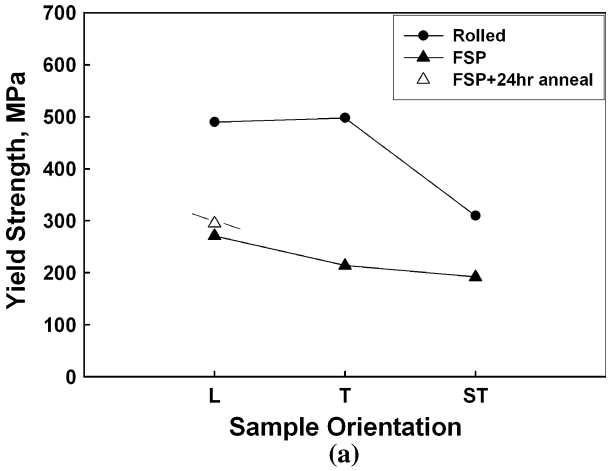

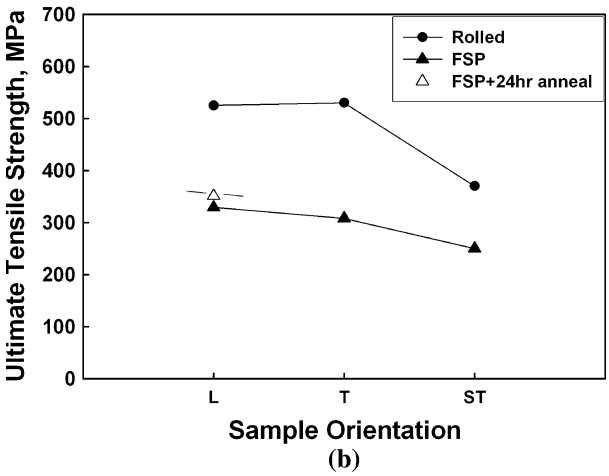

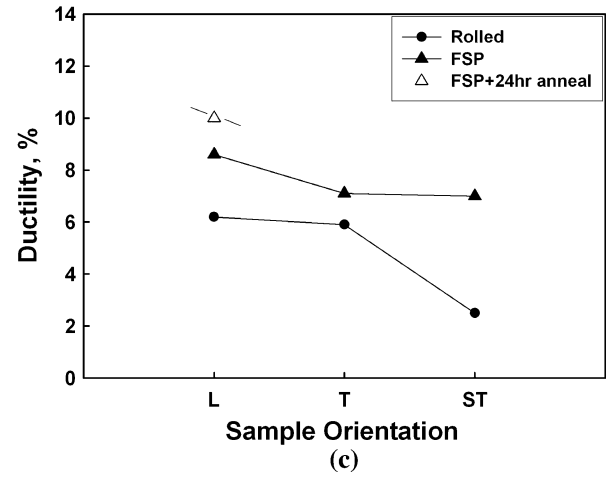

Fig. 5—Plots of (*a*) yield strength, (*b*) ultimate tensile strength, and (*c*) ductility from midplane section along different orientations of the plate for as-received and after-FSP material. Also included are corresponding data from longitudinal orientation of material subjected to FSP followed by annealing at 148 °C for 24 h.

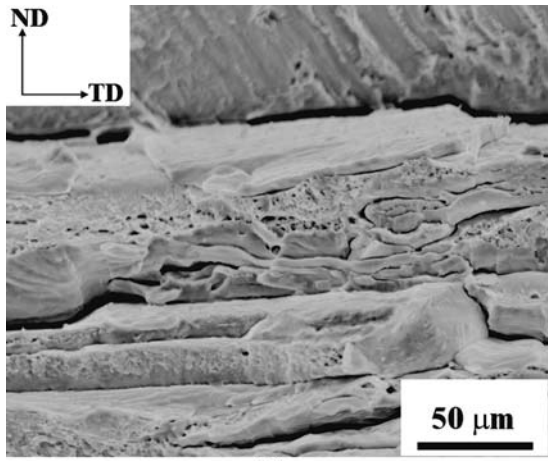

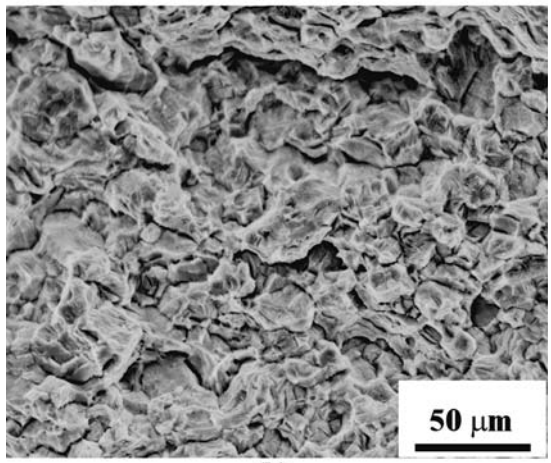

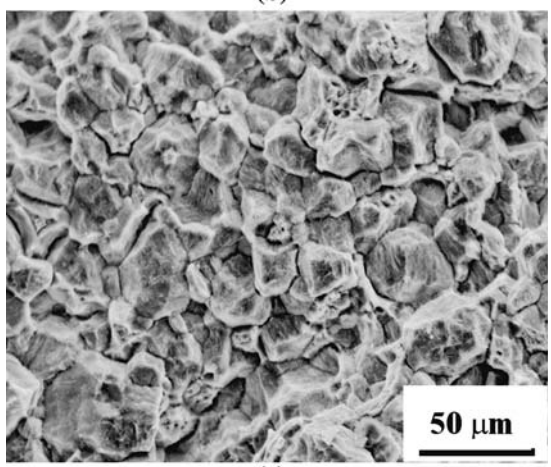

Fig. 6—SEM fractographs of tensile specimens for (*a*) as-received material, (*b*) after FSP, and (*c*) FSP followed by annealing at 148 °C for 24 h.

load range, which resulted in a maximum stress equal to the L orientation yield stress. In contrast, material processed by FSP or by heat treatment following FSP appears to require a stress ~1.7 times the yield strength. Though FSP samples had a lower lifetime at higher loads, the postprocessing heat treatment improved the lifetime to near that of the as-received sample at these loads. Overall, for the entire range of loads studied, FSP appears to improve the fatigue response in anticlastic bending.

The fracture mode during cyclic testing in anticlastic bending is altered by prior FSP (Figures 8 and 9). The

Table II. Number of Cycles-to-Failure at Various Loads for Anticlastic Samples

Sample Condition	3338 N (750 lbs)	4451 N (1000 lbs)	6676 N (1500 lbs)
As-received sample	78,000	10,700	705
FSP	190,000	10,900	140
FSP followed by heat treatment	170,000	10,300	615

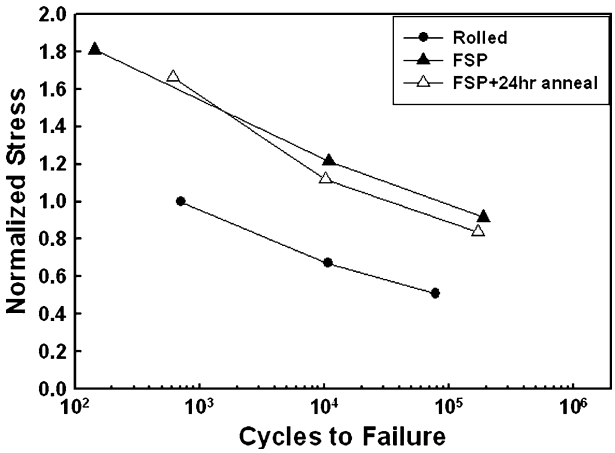

Fig. 7—Normalized stress (failure stress/yield stress) *vs* cycles-to-failure for anticlastic specimens prepared from as-received material, after FSP, and FSP followed by annealing at 148 °C for 24 h.

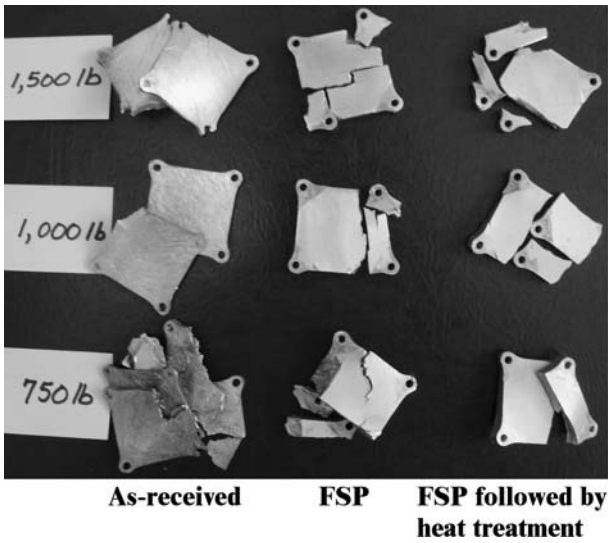

Fig. 8—Photograph of anticlastic test specimens after failure at various loads. From left to right are as-received, FSP, and FSP + HT failed plates, respectively.

macrophotograph of Figure 8 shows all nine samples after testing-to-failure in anticlastic bending. A careful examination of the as-received samples reveals that each of these samples failed on its midplane. This likely reflects delamination cracking due to cyclic shear at this

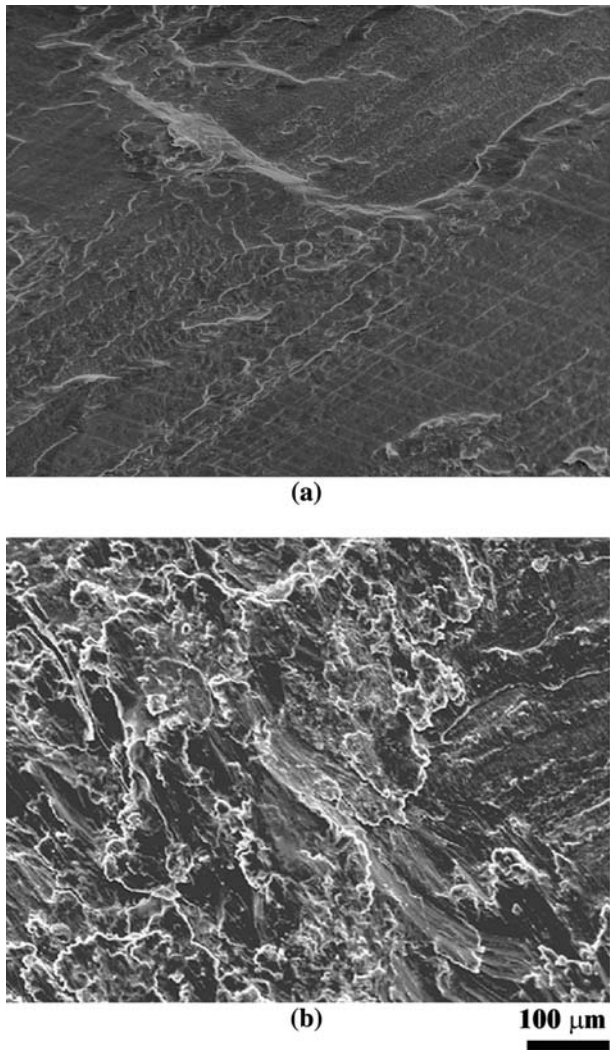

Fig. 9—SEM fracture surface of (*a*) as-received material perpendicular to ND direction and (*b*) FSP material perpendicular to midplane.

location. A crossing pattern of striations in Figure 9(a) from the midplane crack surface of as-received material reflects crack propagation primarily along a direction transverse to that of rolling. In contrast, cyclic anticlastic bending failure occurred in a plane perpendicular to the rolling plane for material subjected to FSP as well as post-FSP heat treatment, suggesting cracking in response to tensile stresses at the sample surface followed by propagation inward toward the midregions (Figure 8). The SEM fractograms show predominately intergranular separation along with small regions having closely spaced fatigue striations (Figure 9(b)) in material subjected to FSP; similar features were apparent after heat treatment of the FSP material.

IV. DISCUSSION

After FSP, the elongated pancake-shaped grains in the as-received material were replaced by refined

equiaxed grains in the stir zone (Figures 1 and 2). In general, the details of the transients and gradients in strain, strain rate, and temperature remain to be determined for the thermomechanical cycle associated with FSP and welding. For FSP applications, estimates of peak stir zone temperatures are in the range of 400 °C to 550 °C for Al-Li alloys. The highest peak temperatures are found at the top of the stir zone in locations nearest the tool shoulder, and peak temperature tends to decrease with depth in the stir zone.[13] Thus, gradients in temperature as well as in strain and strain rate may account for the variation in grain size from the top to bottom of the stir zone (Figures 2(b), (c), and (d)). The largest grains are seen near the top surface of the stir zone and the grain size decreases with depth into the stir zone. The material being processed must be placed on an anvil in order to react the forces associated with FSP. The anvil serves as a heat sink, and therefore the smaller grain size at the bottom of the stir zone reflects a thermomechanical cycle involving lower peak temperatures and shorter dwell times at any temperature below the peak value during the processing. Finally, the rectangular spiral raster pattern employed in the FSP in this investigation will subject any region in the material to multiple thermomechanical cycles. Consequently, grain sizes observed here may be coarser than those expected after a single pass.

The pole figure data also reflect gradients in that distinct shear textures are apparent at the surface and midregions, while the bottom of the stir zone exhibits weaker shear components and a distinct random component in the texture. The presence of a deformation texture in the stir zone is consistent with microstructure evolution by dynamic recovery (DRV) and geometric dynamic recrystallization (GDRX).[20] The DRV takes place readily during hot working of high stacking fault energy metals such as aluminum, and leads to the formation of equiaxed subgrains. Alloying of aluminum does not reduce the stacking fault energy and so DRV is expected to predominate during hot working of aluminum alloys. During DRV, the flow stress, dislocation structure, and texture and its evolution depend on the Zener–Hollomon parameter $Z = \dot{\varepsilon} \exp(Q/RT)$, where $\dot{\varepsilon}$ is the strain rate, Q is the appropriate activation energy, and R and T have the usual meaning. Deformation textures form and persist throughout deformation by DRV although the relative strengths of various texture components will depend on Z. While the prior grains retain their identity at small and moderate strains, they may be reduced in dimension to the subgrain size at very large strains, *e.g.*, such as those encountered during FSP. The prior boundaries become serrated as they respond to the interfacial tensions of the subgrain boundaries and develop waviness over distances on the order of the subgrain size. Then GDRX occurs when the prior boundary separation becomes equal to the subgrain size, which is related to Z^{-1}. Higher peak temperatures near the tool shoulder will then result in coarser grains at the top of the stir zone and finer grains lower in the stir zone when microstructure evolution is dominated by GDRX. Thus, the recrystallized grains are surrounded by a mixture of prior boundary segments and subgrain boundaries. The low-angle peaks in the boundary misorientation distributions in Figures 2(b) and (c) may reflect these subgrain boundaries, consistent with GDRX. Also, because GDRX does not involve long-range migration of high-angle boundaries, the prior deformation texture is retained during the transformation to a recyrstallized state. The addition of Zr as well as the Li in AA2099 may lead to the predominance of GDRX in microstructure evolution within the stir zone in the present investigation.

The appearance of a random texture component at the bottom of the stir zone (Figure 2(d)) may reflect a contribution of particle stimulated nucleation (PSN).[20,21] This involves the formation and growth of new grains from cells or subgrains in the deformation zones that form around nondeforming particles in the microstructure. Lower recovery rates due to higher values of Z may facilitate formation of fine cells or subgrains in deformation zones surrounding nondeforming constituent particles, and thus the PSN reaction. Because the cells or subgrains that form around particles tend to have random orientations, the textures formed by PSN tend to be random.

In the as-received material, TEM showed the presence of fine δ' as well as $\{111\}\alpha$ platelet precipitate formation and some precipitation along grain and subgrain boundaries (Figure 3(a)). Following FSP, the fine δ' dispersion reverted to solution, reflecting stir zone temperatures ≥400 °C. However, TEM data in Figure 3(b) illustrate an increase in size and number of $T1$ precipitate. The presence of $T1$ platelets after FSP suggests a competitive reprecipitation of $T1$ at the expense of other precipitates that would depend on the kinetics and availability of nucleation sites. In fact, $T1$ precipitation dominates that of the other phases, θ'/θ' and δ', in competition for solute (Cu and Li) when heterogeneous nucleation sites are available.[8] Then, reprecipitation of δ' takes place during post-FSP heat treatment (Figure 3(c)).

Processing effects on the precipitation, solid-solution, grain size, and strain hardening mechanisms will combine to determine the strength of this alloy at each stage examined in the current investigation. The hardness and hardness distribution in the as-received plate (Figure 4) reflect mainly cold prestraining and δ' precipitation in the –T8 tempering treatment. Subsequently, the thermomechanical cycle of the FSP has resulted in softening of the stir zone and also in a hardness gradient with depth into the stir zone below the tool shoulder. Overall, the softening reflects the resolutionizing of the δ', as seen in comparison of Figures 3(a) and (b), as well as the annealing of dislocation structures that had been introduced by prestraining prior to aging. Any contributions of grain refinement to strengthening are insufficient to offset these annealing effects. Then the hardness gradient after FSP would reflect residual strain hardening due to the action of the shoulder on the surface as the tool moves through the material. The population of low-angle (<5 deg) boundaries is slightly greater in Figure 2(b) than in either Figure 2(c) or (d) and this may be a consequence of this effect of the tool shoulder. Following a brief 0.24-hour anneal at 148 °C, the hardness near the surface decreases from 57 to 30

HRB, while there is no apparent change in hardness at the bottom of the stir zone. This is consistent with reversion of δ' as well as recovery of the residual strain hardening associated with the tool shoulder prior to the onset of reprecipitation of δ'. Such tool shoulder effects are absent at locations lower in the stir zone. With increasing post-FSP aging, the hardness of the stir zone then increases due mainly to reprecipitation of the δ' (Figure 3(c)). The formation of grain boundary T_1 during the thermomechanical cycle of the FSP reduces the amount of Li available to form δ' during post-FSP aging, contributing to lower strengths after such reaging when compared to the –T8 condition of the as-received material.

Figure 5 summarizes the effect of FSP on the orientation dependence of mechanical properties in this AA2099 material. The as-received –T8 condition exhibits distinctly lower values of both strength and ductility in the ST orientation. The effect of FSP is to reduce stir zone yield and ultimate strengths (consistent with the hardness data) and increase tensile ductility relative to the as-received material. Strength reductions are relatively greater for the L and T orientations than for the ST orientation, while the ductility improvement is greatest for the ST orientation, leading to nearly isotropic tensile properties in processed material. This reflects the replacement of the pancake grain structure of the as-received material with equiaxed grains in processed material (Figures 1 and 2). However, the processing also alters failure modes. In Figure 6(a), separation occurred on boundaries parallel to the plate surface, leading to a layered appearance of the fracture surface accompanied by localized necking and microvoid formation and coalescence in the layer grains. In contrast, the fracture surface of a corresponding tensile sample from the stir zone after FSP exhibits equiaxed grain facets, suggesting a predominance of intergranular failure as well as some microvoid formation and coalescence (Figure 6(b)). Reaging at 148 °C for 24 hours following FSP improves both strength and ductility relative to the FSP sample but the fracture has now become entirely intergranular in nature (Figure 6(c)).

Finally, anticlastic bending tests indicated that the normalized fatigue strength is significantly enhanced after FSP and post-FSP reaging (Figure 7). This improvement in fatigue resistance is accompanied by a change in fracture mode as well. The as-received material failed by delamination cracking on the midplane of each of the test specimens, with crack initiation and propagation in response to the maximum shear on the midplane. The delamination cracking is clear in the photographs of the failed specimens in Figure 8 and in the crossing striation pattern in the fractograph in Figure 9(a). The FSP has eliminated the tendency for delamination in this AA2099 material (Figures 8 and 9(b)). Instead, these samples appear to have failed by crack initiation and propagation in response to the maximum normal stress on planes perpendicular to the plate surface. This, in turn, reflects three processing-related effects: (1) the replacement of the flattened pancakelike grains of the as-received plate with fine equiaxed grains in the processed material, (2) an increase in coarse precipitation, and (3) a change in texture and boundary misorientation distribution in the stir zone. An important factor thought to contribute to delamination in these alloys is the δ'-induced planar slip, which terminates at grain boundaries. The TEM analysis of the FSP plate indicated the resolutionizing of δ', followed by its reappearance after post-FSP heat treatment. Along with the change in grain morphology, the resolutionizing of the δ' may account for the FSP anticlastic bending sample failing in response to the maximum normal stress parallel to the loading direction and not by delamination. Since subsequently heat-treated samples also failed in response to the normal stress, despite having reprecipitation of δ', the change in grain morphology is the predominant factor in altering the failure mode in fatigue. Strong textures and the grain morphology of rolled aluminum lithium alloys also affects in-plane anisotropy.[9] The shear texture in the equiaxed and finer microstructure after FSP may also be a factor, although the role of shear textures in mechanical anisotropy and in fracture mode requires further investigation.

V. CONCLUSIONS

The following conclusions may be drawn from this investigation into FSP of AA2099-T8 plate material.

1. Friction stir processing may be employed to process large areas of sheet and plate products.
2. The elongated pancakelike grains typically produced in conventional thermomechanical processing of this alloy are replaced by equiaxed grains during FSP.
3. The persistence of a shear type deformation texture in the stir zone reflects DRV and GDRX during FSP of this alloy.
4. The thermomechanical cycle of FSP causes resolutionizing of the strengthening δ' precipitates when processing is conducted on material in the –T8 temper. This results in softening of the stir zone although strain hardening may be induced by the tool shoulder, partially offsetting softening due to resolutionizing.
5. Post-FSP aging leads to reprecipitation of δ', but the formation of T_1 during the thermomechanical cycle of the FSP likely reduces the strengthening attainable during such reaging.
6. Friction stir processing leads to mechanical isotropy, especially by improving ST ductility.
7. Friction stir processing alters failure modes, especially in anticlastic bending. The as-received plate fails by delamination cracking of the pancakelike grains in response to the maximum shear on the plate midplane, while the processed material fails in response to the maximum normal stress in planes perpendicular to the plane of the plate. Cracking is still intergranular in nature, as reflected in the presence of grain boundary facets on the fracture surface.

ACKNOWLEDGMENTS

The authors acknowledge the partial support of the Defense Advanced Research Projects Agency (DARPA), Dr. Leo Christodoulou, program monitor, and the Office of Naval Research (Contract No. N00014-06-WR-2-0196), Dr Julie Christodoulou, program monitor.

APPENDIX

Anticlastic bending fatigue testing is a severe procedure for simulating loading encountered by aircraft structural components as well as pressure vessels for cryogen containment. A schematic of a square plate test sample is shown in Figure A1(a). Two equal but opposite bending moments, M and $-M$, are produced at the ends of two diagonals (Figure A1(b)) that result in a pure biaxial bending of the plate with the two principal curvatures having opposite signs.[22] During testing, the state of stress on the surface of the plate is biaxial tension-compression due to the normal stresses. These normal stresses along the x direction are given by

$$\alpha(x, y) = Pxy/I \qquad [A1]$$

where $2P$ is the applied load, x is the distance from the center of the sample to the edge along the diagonal, y is the distance from the midplane (neutral surface) to the top or bottom surface, and I is the second moment of area (*i.e.*, the moment of inertia of the cross section resisting moment). The normal stresses increases linearly in magnitude from the midplane ($y = 0$) to the outer surface along the thickness of the sample (Figure A1(c)). In addition to normal stresses, the sample also experiences reversed shear stresses along the thickness during testing. The shear stresses $\tau(y)$ experienced during anticlastic testing is given as

$$\tau(y) = (P/2I)\left[(h/2)^2 - y^2\right] \qquad [A2]$$

where h is the thickness of the plate. The shear varies parabolically from zero at the top and bottom surfaces to a maximum at the neutral surface. These relationships enable a qualitative determination of the inherent ST weakness due to delamination often exhibited by aluminum lithium alloys and a useful comparison to the effect of thermomechanical treatment of the microstructure during FSP.

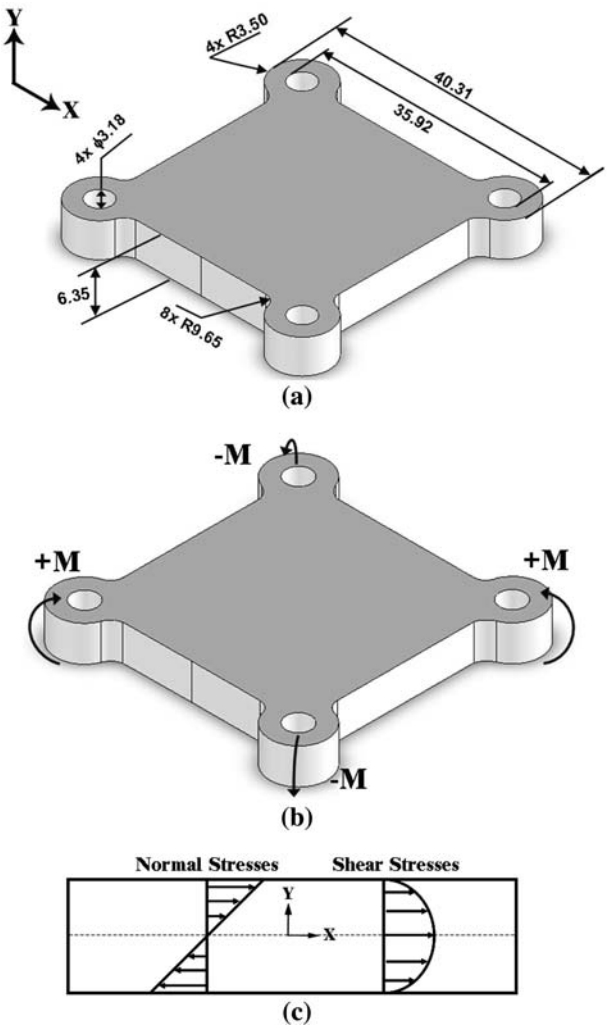

Fig. A1—(*a*) Schematic and dimensions of anticlastic bending samples, (*b*) moments applied to anticlastic bending samples, and (*c*) normal and shear stresses seen along the thickness during anticlastic bending testing.

REFERENCES

1. T.H. Sanders, Jr.: *Aluminum Lithium Alloys*, TMS-AIME, New York, NY, 1981, pp. 63–67.
2. T.H. Sanders, Jr. and E.A. Starke, Jr.: *Aluminum Lithium Alloys II*, TMS-AIME, New York, NY, 1984, pp. 1–15.
3. D.B. Williams: *Aluminum Lithium Alloys*, TMS-AIME, New York, NY, 1981, pp. 89–100.
4. J.E. Kertz, P.I. Gouma, and R.G. Buchheit: *Metall. Mater. Trans. A*, 2001, vol. 32A, pp. 2561–73.
5. A.A. Csontos and E.A. Starke, Jr.: *Metall. Mater. Trans. A*, 2000, vol. 31A, pp. 1965–76.
6. B. Noble and S.E. Bray: *Acta Mater.*, 1998, vol. 46, pp. 6163–71.
7. M.H. Flower and P.J. Gregson: *Mater. Sci. Technol.*, 1987, vol. 3, pp. 81–90.
8. B.M. Gable, A.A. Csontos, and E.A. Starke, Jr.: *J. Light Met.*, 2002, vol. 2, pp. 65–75.
9. K.K. Cho, Y.H. Chung, C.W. Lee, S.I. Kwun, and M.C. Shin: *Scripta Mater.*, 1999, vol. 40, pp. 651–57.
10. N. Eswara Prasad, K.S. Prasad, S.V. Kamat, and G. Malakondaiah: *Eng. Fract. Mech.*, 1995, vol. 51, pp. 87–96.
11. R. Yoshimura, T.J. Konno, E. Abe, and K. Hiraga: *Acta Mater.*, 2003, vol. 51, pp. 2891–2903.
12. R. Yoshimura, T.J. Konno, E. Abe, and K. Hiraga: *Acta Mater.*, 2003, vol. 51, pp. 4251–66.
13. R.S. Mishra and Z.Y. Ma: *Mater. Sci. Eng. R*, 2005, vol. 50, pp. 1–78.
14. M.D. Fuller, S. Swaminathan, A.P. Zhilyaev, and T.R. McNelley: *Mater. Sci. Eng. A*, 2007, vol. 463, pp. 128–37.
15. A.P. Zhilyaev, K. Oh-ishi, G.I. Raab, and T.R. McNelley: in *Ultrafine Grained Materials IV*, Y.T. Zhu, T.G. Langdon, Z. Horita, M.J. Zehetbauer, S.L. Semiatin, and T.C. Lowe, eds., TMS, Warrendale, PA, 2006, pp. 113–18.
16. T.R. McNelley, D.L. Swisher, and M.T. Perez-Prado: *Metall. Mater. Trans. A*, 2002, vol. 33A, pp. 279–90.
17. T.R. McNelley, S. Swaminathan, and J.Q. Su: *Scripta Mater.*, 2008, vol. 58, pp. 349–54.

18. P.B. Prangnell and C.P. Heason: *Acta Mater.*, 2005, vol. 53, pp. 3179–92.
19. R.W. Fonda, J.F. Bingert, and K.J. Colligan: *Scripta Mater.*, 2004, vol. 51, pp. 243–48.
20. F.J. Humphreys and M. Hatherly: *Recrystallization and Related Annealing Phenomena*, Elsevier, Oxford, United Kingdom, 2004, pp. 293–304 and 451–67.
21. F.J. Humphreys and P.N. Kalu: *Acta Metall. Mater.*, 1990, vol. 38, pp. 917–30.
22. S.Y. Zamrik, and R.E. Ryan: in *Advances in Fatigue Lifetime Predictive Techniques*, STP 1292, M.R. Mitchell and R.W. Landgraf, eds., ASTM, West Conshohocken, PA, 1996, vol. 3, pp. 161–87.